Waveform effects on shear wave splitting near fault zones

J. Hua[1,2,3,4], V. Schulte-Pelkum[5], T. W. Becker[2,6,7], B. He[8], H. Zhu[9]

[1]Laboratory of Seismology and Physics of Earth's Interior, School of Earth and Space Sciences, University of Science and Technology of China, Hefei, Anhui, China
[2]Institute for Geophysics, Jackson School of Geosciences, The University of Texas at Austin, Austin, TX, USA
[3]State Key Laboratory of Precision Geodesy, University of Science and Technology of China, Hefei, Anhui, China
[4]Mengcheng National Geophysical Observatory, University of Science and Technology of China, Mengcheng, Anhui, China
[5]Cooperative Institute for Research in Environmental Sciences, University of Colorado Boulder, Boulder, CO, USA
[6]Department of Earth and Planetary Sciences, Jackson School of Geosciences, The University of Texas at Austin, Austin, TX, USA
[7]The Oden Institute for Computational Engineering & Sciences, The University of Texas at Austin, Austin, TX, USA
[8]Department of Earth, Atmospheric, and Planetary Sciences, Purdue University, West Lafayette, IN, U.S.A.
[9]Department of Earth and Space Sciences, Southern University of Science and Technology, Shenzhen, Guangdong, China

Key Points:

- Shear zones wider than 80 km can be clearly detected by shear wave splitting
- Scattering causes erroneous delay times and apparent fast axes approaching the incidence azimuth near the edge of the shear zone
- Good azimuthal coverage is critical for the investigation of fault zones with shear wave splitting

Corresponding author: Junlin Hua, junlin_hua@ustc.edu.cn

Abstract

Shear wave splitting of teleseismic core phases such as *SKS* is commonly used to constrain mantle seismic anisotropy, a proxy for convective deformation. In plate boundaries, sharp lateral variations of splitting measurements near transform faults are often linked to deformation within a lithospheric shear zone below, but potential seismic waveform effects from heterogeneous structure on small scales may influence the interpretation. Here, we explore possible finite frequency effects on shear wave splitting near fault zones in a fully three-dimensional anisotropic setting. We find that shear zones wider than ∼80 km, a scale set by the Fresnel zone, can be clearly detected, but narrower zones are less distinguishable. Near the edge of the shear zone, the combined effect of anisotropy and scattering generates false splitting measurements with large delay times and fast axis orientation approaching the back-azimuth, a bias which can only be identified when records from different back-azimuths are analyzed together. This substantiates that back-azimuthal variations of splitting can arise not just from vertical layering but also lateral changes of anisotropic media. We also test the effects of shear zone edge geometry, epicentral distance, filtering frequency, crustal thickness, and sediment cover. Our study delineates the ability of shear wave splitting to resolve and investigate fault zones, and emphasizes the importance of good azimuthal coverage to correctly interpret observed anisotropy. Based on revisiting previous shear wave splitting and lithospheric deformation studies, we infer that many crustal fault zones are underlain by lithospheric shear zones at least 20 km wide.

Plain Language Summary

When an earthquake occurs, elastic waves are generated and pass through the Earth's interior. If the rock is deformed, effectively anisotropic properties can arise where a seismic wave can be split into two pulses that vibrate in different orientations and propagate with different speeds. Thanks to this wave birefringence-like phenomenon, the deformation of the Earth's interior can be better understood by analyzing seismic waves recorded at the surface. Near fault zones, where different tectonic blocks move with respect to each other, splitting is often observed, indicating deformation exists below the surface in the fault zone. In this study, by numerically modeling wave propagation, we study the capability to decode such deformation around fault zones based on this wave splitting phenomenon. The results show that for deformation zones over 80 km wide, the wave splitting phenomenon can be clearly detected. However, near the edge of the deformation, biased measurements of splitting can appear, leading to erroneous interpretations. Other factors that could influence the splitting measurement around fault zones are also studied. By comparing the results with previous studies, we substantiate that many observed splitting variations are likely due to deep lithospheric shear zones wider than 20 km.

1 Introduction

Strike-slip faults are major components of how plate tectonics is expressed on the surface, and continental transforms such as the San Andreas, Alpine, and Anatolian fault zones pose major hazards to society. How deformation is localized in these plate boundaries and how such systems evolve remains debated. Most shallow transform deformation occurs by brittle failure, but how transform faults transition to ductile shear deformation at depths is not clear (e.g. Sibson, 1983; Norris & Toy, 2014). Modeling analysis of oceanic (Behn et al., 2002) and continental (Allison & Dunham, 2021) transforms indicates ∼ 50 km wide ductile shear zones underneath the brittle domain. Similar width transitions in deep crustal structure are seen along the San Andreas (Ford et al., 2014), albeit with complications due to laterally variable lithology.

To investigate deformation within the Earth's interior, seismic anisotropy has long been viewed as a reliable proxy. Intrinsically anisotropic minerals within rocks can align under finite strain, causing effective anisotropy via crystallographically preferred orientation (CPO), or different isotropic wave speed media can align, leading to shape preferred orientation (SPO). Both types of anisotropy cause seismic waves propagating and/or vibrating in different orientations to exhibit different velocities (e.g. Silver, 1996; Long & Becker, 2010). A common simplification of seismic anisotropy is azimuthal anisotropy (e.g. Montagner & Anderson, 1989), characterizing the azimuthal dependence of seismic velocities. To observe it, analysis of shear wave splitting of teleseismic core phases is one of the most common methods (Ando et al., 1983; Vinnik et al., 1984; Silver & Chan, 1991). Due to the outer core being liquid, only compressional waves can travel within it, and when exiting the core, seismic shear phases converted at the core-mantle boundary (e.g., *SK(K)S, PKS*) are thus only polarized in the radial orientation with no transverse energy, and these phases are hereafter referred to as *XKS* phases. Hence, if transverse motion is present at the station, it is likely due to seismic anisotropy along the path from the core-mantle boundary to the station, thus, by performing shear wave splitting on these phases, it is possible to quantify the cumulative effect of azimuthal anisotropy (e.g. Montagner et al., 2000; Becker et al., 2012).

A number of studies have analyzed shear wave splitting around strike-slip fault systems (e.g. Hartog & Schwartz, 2001; Little et al., 2002; Rümpker et al., 2003; Savage et al., 2004; Biryol et al., 2010; Zietlow et al., 2014; Barak & Klemperer, 2016; Jiang et al., 2018; Gao et al., 2019; Merry et al., 2021; Bolton et al., 2022), and many have observed lateral variations in splitting parameters with fast axis orientations rotated and aligned with the fault strike near the fault (Monteiller & Chevrot, 2011; Bonnin et al., 2012; Zietlow et al., 2014; Jiang et al., 2018; Merry et al., 2021). Due to the short spatial scale of many of these variations, these lateral changes are often interpreted to be seismic anisotropy changes within the lithosphere where the sensitivity, expressed by the Fresnel zone width (Rümpker & Ryberg, 2000; Chevrot et al., 2004; Long et al., 2008; Monteiller & Chevrot, 2010) is more localized, and are hence linked to potential deformation within the lithospheric shear zone. However, the three-dimensional nature of the shear zone may complicate seismic waveforms, potentially making the common one-dimensional shear wave splitting interpretation inappropriate. While a number of studies have been conducted to analyze shear wave splitting measurements around shear zones with two/three-dimensional geometry (Savage et al., 2004; Chevrot et al., 2004; Kaviani et al., 2011; Bonnin et al., 2012; Reiss et al., 2016; Rümpker et al., 2023), they are usually targeted to specific settings rather than a study of general waveform effects due to the shear zones.

Here, we systematically analyze the finite-frequency effect of shear zones on shear wave splitting. We generalize the seismic structure around fault zones into idealized models, obtain corresponding synthetic seismograms using a three-dimensional seismic wave propagation solver (Komatitsch & Tromp, 2002; Monteiller et al., 2021), and perform shear wave splitting measurements on these synthetic data. With these synthetic measurements, we (1) test the capability of *XKS* shear wave splitting to detect a shear zone, including its width and its magnitude of anisotropy; (2) analyze the possible three dimensional influence that shear zone structure contributes, and how these would affect measurements; (3) investigate relevant factors such as shear zone edge geometry, crustal thickness and waveform frequency content and their influence on the detectability of the shear zones; and (4) discuss the impact of the findings on the interpretations of real observations.

2 Model Setup

To investigate the ability of *XKS* shear wave splitting to detect structures around faults, a generalized model around a strike slip fault is constructed (Figure 1). The model contains three layers, a crust, a mantle lithosphere, and an asthenosphere. Within the

brittle crust, fault slip zones are often limited to < 1 m wide while damage zone widths are under a few hundred meters (Y.-G. Li & Leary, 1990; Yang et al., 2011; Cocco et al., 2023), much less than the Fresnel zone width of seismic waves which is around 50-100 km depending on specific frequency ranges (Rümpker & Ryberg, 2000; Long et al., 2008; Monteiller & Chevrot, 2010). Therefore, the crustal part of the fault is assumed to be infinitely narrow in the model, and the crust is set to be isotropic with a shear velocity (V_S) of 3.85 km/s, a compressional velocity (V_P) of 6.5 km/s, and a thickness marked as h_c, which in most cases is 35 km. In one of the tested models, an isotropic sedimentary basin is included, extending from the surface to a depth of h_s, with a width of w_s centered at the fault. Following Kaviani et al. (2011), its V_S is 2.7 km/s, and V_P is 4.8 km/s.

Mantle shear zones with widths ranging from a few tens to a few hundreds of kilometers have been inferred beneath strike-slip faults (Martelat et al., 1999; Vauchez et al., 2012; Ford et al., 2014; Norris & Toy, 2014; Hua et al., 2018). In this study, above the asthenosphere, a "sandwich" model is assumed for the mantle lithosphere with two off-shear zone side blocks and an anisotropic shear zone in between (Figure 1). The two mantle lithospheric blocks have thicknesses of h_l and h_r to accommodate possible changes in lithospheric thickness across the shear zone. The shear zone in between has a width of w, and its lithosphere-asthenosphere boundary (LAB) connects the LABs of the side blocks. Measured anisotropy variations are assumed to be mainly due to lateral changes in the mantle lithosphere. However, if ductile deformation within the lower crust were the source of the anisotropy variation, the general results would still be similar, given that the mantle lithosphere layer in the tested model plays a role similar to that of the lower crust. We also examine the effect of a ductile lower crust by including an anisotropic lower crustal shear zone with thickness h_{lc} and width w_{lc}, as well as testing the influence of a dipping/gradual shear zone-side block transition (Section 4.3).

To represent mantle anisotropy, olivine elasticity is assumed. Following Browaeys and Chevrot (2004), the olivine elastic tensor can be decomposed into isotropic, transversely isotropic (TI, or "hexagonal"), tetragonal, and orthorhombic components, and only its isotropic component C^I ($C^I_{11} = C^I_{22} = C^I_{33} = 194.7\,GPa$, $C^I_{12} = C^I_{13} = C^I_{23} =$ 67.3 GPa, $C^I_{44} = C^I_{55} = C^I_{66} = 63.7$ GPa, in Voigt notation), and transversely isotropic component C^{TI} ($C^{TI}_{11} = C^{TI}_{22} = -21.7$ GPa, $C^{TI}_{33} = 77.3$ GPa, $C^{TI}_{12} = 1.7$ GPa, $C^{TI}_{13} = C^{TI}_{23} = -9.3$ GPa, $C^{TI}_{44} = C^{TI}_{55} = -2.7$ GPa, $C^{TI}_{66} = -11.7$ GPa) are used in this study. The combined elastic tensor for mantle materials C is defined as $C^I + \gamma C^{TI}$, where γ regulates the anisotropy strength, assuming Voigt averaging. Within the shear zone, γ is set to unity, corresponding to 7.9% anisotropy. In isotropic parts of the model, γ is set to zero. If the asthenosphere is anisotropic, γ is set to 0.25 to ensure its weaker contribution to splitting measurements than the shear zone, given observed fault-parallel fast-axes suggest a potentially stronger contribution from the lithosphere (e.g. Zietlow et al., 2014; Jiang et al., 2018; Gao et al., 2019) and the asthenosphere in the model is thicker than the lithosphere. If side blocks are anisotropic, their γ is set to 0.5 because they likely experienced less deformation than the shear zone. For the case with a lower crustal shear zone, γ is set to 0.6 and C^{TI} is added to the isotropic elastic tensor of the crustal material for the lower crustal shear zone, so that 6.9% anisotropy would be present. For the original form, the elastic tensor shows transverse isotropy with vertical symmetry axis, and no azimuthal anisotropy is expected. Hence, the tensor is first rotated 90° around a horizontal axis to generate fast and slow axes on the horizontal plane. Then, in most cases, the tensor is rotated with respect to the vertical axis to have its fast axis pointed to the North for the shear zone, and N45°W for the side blocks and the asthenosphere if they are set to be anisotropic to explore variations in fast axes.

Surface seismic stations are always linearly aligned in the East-West orientation (Figure 1). The station spacing is 1 km, and they are centered on the fault. The angle between the station alignment and the fault strike (α) is mostly 90° with the fault extended in the North-South direction, except for one case where the fault strike is N60°W.

3 Methods

3.1 Wavefield simulation

To account for full three-dimensional finite frequency effects, the wavefield was calculated using the spectral element method (Komatitsch & Tromp, 2002). To enable the injection of a plane wave to mimic teleseismic *SKS* phases, a variant version of the wavefield simulation tool SPECFEM3D Cartesian (Komatitsch & Tromp, 2002), RegHyM (Monteiller et al., 2021), was used. The incident plane wave was injected using the frequency-wavenumber method (Tong et al., 2014), and to represent an *XKS* phase, only SV motion is excited. The incidence angle at the bottom is mostly set to 10°, corresponding to a ray parameter of 0.039 s/km, equivalent to an *SKS* arrival from a shallow earthquake with an epicentral distance of 107° (Kennett & Engdahl, 1991). For each tested model, 18 individual computations were performed for back-azimuths ranging from 0° to 340° with a 20° interval. If not specifically mentioned, the source time function was characterized by a Gaussian wavelet with a central period of 5 s.

The simulation was performed in a box with a dimension of 800 km (East-West) $\times$ 600 km (North-South) $\times$ 200 km (vertical). This box size ensures that all stations are at least 300 km away horizontally from the boundary to avoid boundary reflection effects. 50 elements were set vertically and in the North-South direction. Since the fault strike is mostly North, no N-S lateral variation is expected, so 42 elements were used to guarantee a minimum resolved period of less than 5 s. Along the East-West orientation, the mesh size varies depending on the shear zone width, but the shear zone always consists of more than 5 elements at that direction. We computed 7000 time step simulations with time step of 0.02 s, and each simulation took 5 to 25 minutes depending on mesh size on 60 CPUs.

3.2 Shear wave splitting measurement

To measure shear wave splitting, methods based on cross-correlation (Fukao, 1984), splitting intensity (Chevrot, 2000), and transverse (T) component minimization (Silver & Chan, 1991) have been introduced. In this study, splitting was measured by the T component minimization method, given that it is most commonly used and relatively robust in many cases (Long & Silver, 2009). This method utilizes a grid-search of potential fast-axis orientations and delay times to obtain parameters that could provide minimal energy on the T component before splitting happens. To mimic an actual measurement, the single splitting measurement module in the MATLAB-based SplitRacer toolbox (Reiss & Rümpker, 2017) was used to conduct two standard measurements: 1), the azimuth of the fast propagating pulse ("fast-axis" orientations), as an indication of the orientation of the anisotropic symmetry axes, and, 2), the delay time between slow and fast pulse arrival, as an indication of path-integrated anisotropy strength, as well as their errors.

Basic processing was applied to the synthetic data. The seismograms were bandpass-filtered to 5-100 s, and horizontal components were rotated to radial (R) and T components based on the back-azimuth. A $\pm$11 s time window around the maximum amplitude on the R component was used for analysis, and the measurement was performed based on the R and T components set as defaults in SplitRacer. We also performed the measurement in the LQT coordinate system (Šíleny & Plomerová, 1996) to account for the incidence angle, which produced very similar results that are not further discussed. Only splitting measurements with T energy reduction above 80% are analyzed here, and others are marked as null measurements.

4 Results and Discussion

4.1 The detectability of a shear zone

Shear wave splitting behaviors were examined for shear zones with four different widths of 20, 40, 80, and 120 km. When the back-azimuthal coverage is even, the median splitting measurement of all back-azimuths varies smoothly along the array for all four models. In detail, when the shear zone is narrow (Figure 2a), subtle changes in both fast axis orientation and delay time can be observed. However, due to a Fresnel zone width of over 50 km (Rümpker & Ryberg, 2000; Long & Silver, 2009), the anisotropy influence from the side blocks is overprinted onto seismograms recorded above the shear zone, making it difficult to detect fault zone width and its anisotropy strength purely from the measurements. Individual measurements from different azimuths at a station are very unstable near the fault zone, with varying fast axis orientations and delay times, showing the difficulty of obtaining conclusive measurements in the real world for narrow shear zones (cf. Chevrot et al., 2004). When the shear zone is 40 km wide (Figure 2b), the result is similar to the 20 km case. Though the wider shear zone makes more stations exhibit evidence of the existence of a shear zone, the width is difficult to determine, and no station above the shear zone shows stable measurements from different back-azimuths.

The shear zone becomes more distinguishable when the fault zone has a width of 80 km (Figure 2c). At the center of the shear zone, stations start to show stable splitting measurements from different back-azimuths, indicating that the influence from the side blocks has faded. Because the transition in splitting measurements from the side block to the shear zone happens within ± 40 km of the shear zone edge, it is now possible to determine the width of the shear zone as defined by the center of each transition. The measurements become more stable for a wider shear zone of 120 km (Figure 2d). In this case, stations ± 20 km around the center show identical splitting measurements from different back-azimuths, while stations around the edge of the shear zone behave similarly to ones in the 80 km width case.

Based on these tests, the influence of the edge on shear wave splitting extends $\sim$ 40 km laterally around it, consistent with the Fresnel zone width (Rümpker & Ryberg, 2000), making shear zones wider than 80 km free of edge effects near the center. Models with side block fast axes aligned in the east-west direction show that more drastic change in anisotropy result in the shear zone becoming more distinguishable, and even narrow shear zones ($w = 40$ km) may be detected (Figure S1). However, individual measurements ~ 40 km around the edge are still unstable, and higher inconsistency of measurements is expected from different back-azimuths (Figure S1). These tests also suggest that besides the widely recognized effects of vertical layering and dipping symmetry axes (e.g. Silver & Savage, 1994; Rümpker & Silver, 1998; Chevrot & van der Hilst, 2003), lateral variations in anisotropic properties could also cause strong back-azimuth variations in splitting measurements.

4.2 Edge-induced erroneous measurements

Though measured shear wave splitting parameters vary smoothly across the shear zone when the median value is taken, individual measurements from the same station often present large variations near the edge of the shear zone, and many of them are not aligned with the model anisotropy (Figure 2). To probe the underlying cause behind these peculiar measurements, a specific test was conducted. We use the same model as Figure 2d ($w = 120$ km), but with isotropic side blocks, so that isolated waveform effects of the shear zone can be analyzed.

Based on this test, highly variable measurements are observed near the edge of the shear zone; those result from actual waveform effects, but can be considered erroneous in that the splits are not indicative of any true anisotropic structures (Figure 3a). By

analyzing splitting measurements at different stations from the same back-azimuth, we found that gradual transitions occur from the center of the shear zone to the side blocks, with the measured fast axis orientation approaching the back-azimuth direction from the actual fast axis orientation, and the delay time reducing first and then increasing (Figures 3b, 3c, and S2).

By analyzing the waveforms, we find the transverse motion that leads to the erroneous measurements outside the shear zone to be a combined result of shear zone anisotropy and scattering. Due to the broad Fresnel zone and the anisotropy within the shear zone, even if the station is situated outside of the shear zone, transverse motion still occurs although weaker than at the center of the shear zone (Figures 4a to 4d). Meanwhile, part of the transverse motion is also caused by a pure scattering effect. In a separate test with a shear zone that is isotropic with an V_S same as the slow axis velocity of the previously tested anisotropic shear zone, transverse motion due to scattering appears outside of the shear zone (Figures 4r to 4t). Overall, the typical shape of the T component (proportional to the derivative of the R component, Figures 4b to 4d) as expected for shear wave splitting (Silver & Chan, 1991) is mainly the result of the shear zone anisotropy, but the delayed arrival time leading to large apparent splitting delays is likely caused by the scattering effect (Figure 4).

The reason why the fast axis orientation of these erroneous splitting measurements approaches the back-azimuth (Figure 3b) is due to the small transverse motion. The amplitude of scattered seismic waves decreases due to the geometric spreading effect, and the farther from the shear zone, the weaker the corresponding T motion is. Based on the T component minimization method (Silver & Chan, 1991), when the transverse motion is small, the measured fast axis orientation is expected to be close to the radial direction, so that the radial motion multiplied by the sine value of the small angle between the back-azimuth and the measured fast axis is comparable to the transverse motion multiplied by the cosine value of the angle. By adding them up, the first peak on the transverse component is mostly canceled, leaving the slow axis to only present one delayed remaining peak (Figure 4d). Based on the corrected T energy grid-search result, the measured fast axis is close to the back-azimuth orientation, and the error in delay time is large (e.g. Figure 4h). This type of grid-search result is also commonly observed in other settings when the transverse motion is small (e.g. Reiss & Rümpker, 2017).

The reason behind the large splitting delay times (Figure 3c) is mainly a scattering effect. As expected for the longer travel time of scattered waves at stations farther from the shear zone, the peak of the slow axis is delayed with increasing distance from the shear zone (Figures 4f to 4h), resulting in the observed increasing splitting delay times.

Because of the relatively small T motion (e.g., Figure 4d), when anisotropy is present in the side blocks, the scattering influence becomes negligible. However, as T motion gradually decreases with distance, the aforementioned effect can still generate a strong effect near the shear zone (e.g., Figure 4b). Meanwhile, when the back-azimuth is close to the fast/slow axis of the side blocks and the transverse motion generated by the side block anisotropy is also small, erroneous measurements are likely to occur (Figures S3a and S3b, 20°/40° back-azimuth for without/with erroneous measurements).

These tests demonstrate the importance to sample shear wave splitting measurements from a range of back-azimuths, so that erroneous measurements can be distinguished. The aforementioned cause behind erroneous measurements does not only affect observations near fault zones, but also other tectonic settings where two different blocks are juxtaposed (cf. Chevrot et al., 2004).

4.3 The influence of the shear zone to side block edge transition

In nature, the geometry of shear zones is not expected to be as regular as in our example setup of Figure 1 with constant width and sharp edges. As summarized in Norris and Toy (2014), for example, lithospheric shear zones may present different shapes as a function of tectonic background setting and fault network evolution. While it is impractical to explore all potential geometries, less simplified representations of realistic shear zones might be approximated with a combination of dipping shear zone-side block edges and a more gradual shear zone-side block transition. Hence, we test two additional setups that are designed to explore the influence of the shear zone - host rock transition.

First, we test the influence of a dipping shear zone-side block edge (Figure 5a). While this setup is similar to the reference geometry as used for Figure 2c, the shear zone is narrower at the Moho with a width of w_1 and wider at the LAB with a width of w_2, mimicking the broadening of a lithospheric shear zone with depth (e.g. Sibson, 1983). Three cases with w_1 set to 60, 40, 0 km and w_2 set to 100, 120, 160 km were tested to represent different dipping angles, while the average shear zone width is kept at 80 km, as in the reference case. The first case with $w_l = 60$ km and $w_2 = 100$ km (Figure 5b) shows a similar splitting pattern to Figure 2c, with the aforementioned erroneous measurements present (Figures 5b and S3c). In comparison, when the edges are at $w_l = 40$ km and $w_2 = 120$ km in the second case, individual measurements become more consistent (Figure 5c versus 5b), with less influence from artifacts. When the dipping edge takes up 80 km horizontally ($w_l = 0$ and $w_2 = 160$ km; Figure 5d), i.e., a transition comparable to the width of the area where inconsistent individual measurements exist for a vertical edge (e.g. Figure 2c), individual measurements become consistent with little deviation from the mean.

A similar reduction in complexity is observed if the fault zone to side block transition is smooth. For this, we set the center area of the shear zone with $\gamma = 1$ to have a width of w_3; outside, the elastic tensor changes gradually to that of the side block such that the total width affected by anisotropic shear zone is w_4 (Figure 5e). Other parts of the model are identical to the reference case of Figure 2d. Three cases with w_3 set to 100, 80, 40 km and w_4 set to 140, 160, 200 km were tested to represent different transition widths. For the first case where the transition happens within 20 km (Figure 5f), the measured splitting complexity is similar to the sharp transition case with Figure 2d with inconsistent individual measurements around the transition. When the transition width is 40 km (Figure 5g), individual measurements get slightly more consistent, but the erroneous measurements around the transition persists (Figures 5g and S3e). Individual measurement become consistent when the transition width reaches 80 km (Figure 5h), comparable to the width of inconsistent measurements around a sharp edge (e.g., Figures 2d).

Based on the tests, a dipping edge or a gradual transition could both be regarded as a broad horizontal transition from shear zone to side block. When such a transition is comparable to, or wider than, the 80 km width over which inconsistent measurements occur near a sharp vertical edge (e.g., Figures 2d), splitting measurements from different back-azimuths would be consistent near the transition part (Figures 5d and 5h). When the horizontal transition is narrower than such a width, the aforementioned erroneous measurements would occur, causing inconsistent measurements.

4.4 Other factors complicating shear wave splitting around fault zones

Other factors that may influence splitting measurements are tested, including epicentral distance, the period of the source time function, crustal thickness, lower crustal shear zone, sedimentary basins, asthenospheric anisotropy, a dipping LAB, and the station distribution.

To examine the influence of epicentral distance, in two additional tests, the incidence angle was set to 14.9° and 6.5°, equivalent to *SKS* distances of 85° and 130°, the common upper and lower limits for *SKS* analyses (e.g. Jiang et al., 2018). Although *SKKS* phases up to 180° could be used for splitting measurements, its incidence angle would fall into the tested range. When the distance is shorter, the larger incidence angle would cause a slightly broader transition ($\sim$ 45 km around the edge) with more stations showing inconsistent individual measurements from different back-azimuths (Figure 6a), and a longer epicentral distance would bring a shorter transition ($\sim$ 35 km around the edge, Figure 6b). Such difference in transition width could be related to the Fresnel zone's dependence on incidence angle (Chevrot et al., 2004) and the difference in shear zone edge-induced scattering for incoming waves with different incidence angles, suggesting that apart from the Fresnel zone size for a vertically traveling wave, the ray geometry would also affect the resolution width of a shear zone.

For source-time functions with longer periods, due to the wider Fresnel zone, the transition occurs over a longer distance (Figures 6c versus 2c). Events from different back-azimuths are more inconsistent, showing the advantage of using shorter-period waves.

When the crustal thickness is reduced to 10 km, due to the smaller Fresnel zone (Rümpker & Ryberg, 2000), the transition at the shear zone edge takes a shorter distance, and $\sim$ 30 km around the edge shows unstable individual splitting measurements versus $\sim$ 40 km when h_c is 35 km (Figures 6d versus 2c). Because of the shallow Moho, this case could potentially also represent the influence of a lower crustal shear zone, especially for regions like Tibet where the Moho depth is similar to the LAB in this test. Hence, lower crustal shear zones likely need to be wider than 60 km to be confidently identified.

To specifically test the scenario where shear deformation is also accommodated within the lower crust (Sibson, 1983), we tested a case with a 40 km wide and 20 km thick lower crustal shear zone, while other settings are identical to the case in Figure 2c. The splitting measurements (Figure 6e) are similar to Figure 2c despite the center part shows longer delay times due to the additional crustal anisotropy.

Previous studies have shown a significant influence of sedimentary basins around fault zones on shear wave splitting measurements (e.g. Kaviani et al., 2011). Here, this effect is tested by including a 20 km-wide sedimentary basin. Delay times are strongly affected, but not as much for the measured fast-axis orientations (Figures 6f versus 2d), consistent with the findings of Kaviani et al. (2011). Further analysis shows that the sedimentary basin influences measurements for all back-azimuths (Figure S3l), and that delay time is reduced for stations in the sedimentary basin and increased for ones just outside (Figure S4).

When anisotropy also exists beneath the lithosphere, the general conclusions are similar to the case without asthenospheric anisotropy (Figures 6g versus 2c). The most noticeable difference is the expected difference in fast-axis orientation. Because of the deeper anisotropy, events with back-azimuths aligned with the shear zone fast axis can also produce meaningful measurements, but with much larger delay times (Figure 4g). Erroneous measurements due to the shear zone edges (Figure S3m) also appear in this model.

Dipping boundaries are also recognized as a source of complication in anisotropy measurements (Savage, 1998; Frederiksen & Bostock, 2000; Chevrot & van der Hilst, 2003; Levin et al., 2007). We tested the influence of a dipping LAB beneath the shear zone (Figure 6h); resulting synthetics for our tests showed small irregular features, suggesting a minor role of the LAB geometry.

In our previously tested models, the seismic array alignment is always perpendicular to the fault strike, which is not always the case in real experiments. Therefore, us-

ing the actual station distribution across a section of the San Andreas Fault (Jiang et al., 2018) as an example, we tested a case where the angle between the fault strike and the station alignment is 150° (Figure 6i). In this case, the shear zone is only 40 km wide, but because of the 150° angle difference, the east-west array spans 80 km on top of the shear zone (schematic in Figure S5). Fast axes are oriented east-west in both the side blocks and the asthenosphere, with γ set to 0.44 and 0.3, and parallel to the fault in the shear zone with γ set to 1. The result presents a different back-azimuthal dependence around the edge, for example, when the back azimuth is 320° (N40°W), stations west to the shear zone show influence from the shear zone (Figure S3o) while east ones do not, which is not the case when the shear zone is North-South oriented (Figure S3a). This is because in this case, the fault is extended to the northwest, making seismic waves from northwest still sample the shear zone even if the station is west to the shear zone. Meanwhile, thanks to the more extensive coverage over the shear zone, for the same w, more stations show evidence of the shear zone and are in general more consistent than the case where the station alignment is perpendicular to the fault (Figure 6i versus 2b). Hence, if targeting relatively narrow shear zones, deploying stations at angles not perpendicular to the fault could potentially result in improved splitting measurements.

4.5 Comparison with observations

Shear wave splitting measurements have been made across real fault zones for deformation zones with different widths. The Alpine Fault together with the Marlborough fault system on the South Island of New Zealand is a prominent strike-slip fault system. Around it, teleseismic core phase splitting measurements show a shift in fast axis orientation from relative plate motion-parallel offshore to perpendicular to it inland, suggesting a broad shear zone up to 200 km wide (Zietlow et al., 2014), and local splitting measurements confine it to within the lithosphere (Karalliyadda et al., 2015). Recent studies using seismic receiver functions to investigate lithospheric anisotropy in the same region also support such a distributed shear zone (Hua et al., 2018). Based on our tests, such a wide shear zone can be confidently determined with teleseismic shear wave splitting, though detailed shear zone geometry remains to be explored (Norris & Toy, 2014).

Across the Tintina fault in Northwest Canada, the fast axis orientation changes from fault-parallel to North American plate motion direction through a $\sim$ 20 km transition (Mark, 2024). Such transition is consistent with a wide shear zone similar to the Alpine fault.

Across the San Andreas Fault system, the shear zone appears to be narrower. In the northern part of the system, a $\sim$ 40 km wide shear zone is evident from splitting (Bonnin et al., 2012). In the southern part, around the Salton Trough, fault parallel splitting measurements are seen over $\sim$ 100 km width, but may be affected by partial melting (Barak & Klemperer, 2016). In the central part of the system, where the plate boundary is not divided into multiple faults, Jiang et al. (2018) discovered fault-parallel fast axis orientations across $\sim$ 35 km distance, but instead of centered at the fault, these distinctive shear wave splitting measurements are located east to the fault. Based on the synthetic test in this study, for a 35 km wide zone with distinctive splitting measurements, the actual shear zone could be narrower (e.g. Figure 6f), as stations outside the zone can also be influenced. Given that the majority of the earthquakes are from the northwest (Jiang et al., 2018), the actual shear zone could be located further to the east (Figure S3o), suggesting the possibility of a larger offset between the fault and the shear zone beneath. However, while some stations further east show null measurements, some also exhibit fault-parallel fast axes (Jiang et al., 2018), which may indicate a wider shear zone, and the relatively small delay time at $\sim$ 120°E may be due to sediment effects (e.g. Figure 6f). If the region with null measurements is also part of the shear zone, the shear zone may be wider than 100 km, and instead of being an active shear zone of the San Andreas Fault system, the observed splitting pattern could also be due to fossil defor-

mation not aligned with current kinematics (Schulte-Pelkum et al., 2021). Nonetheless, relatively wide lithospheric deformation is likely to exist beneath the fault regardless of the original cause.

Near the strike-slip Longriba fault in Eastern Tibet, fault-parallel splitting is observed within ~ 35 km around the fault (Gao et al., 2019). A $\sim 90^\circ$ abrupt change in fast axis orientation is seen north to the fault, which is supported by our tests when the shear zone width is 40 km (Figure S1b). However, if the shear zone is as narrow as $\sim$ 20 km, null measurements are likely to occur (Figure S1a). Hence, the shear zone is likely between 20 and 35 km wide, and could be located within both the crust and the mantle lithosphere given the deep Moho (Gao et al., 2019).

Sharp spatial splitting parameter variations are evident in the western part of the North Anatolian Fault. There, ~ 20 km wide fault-parallel splitting features are observed by a dense array (Merry et al., 2021), with a $\sim 45^\circ$ change compared to neighboring stations. Since seismic anisotropy starting at 10 km depth and extending deeper would still show an effect 30 km away (Figure 6d), the lateral variations have to occur in the uppermost crust, but the large delay time then becomes difficult to explain. We note that these measurements come from a few stations with a limited number of individual measurements and relatively small differences between the back-azimuth and the measured fast axis, which might suggests the effect documented in Section 4.2. The overall fast axes around the North Anatolian Fault are not fault-parallel and might be affected by mantle flow not disrupted by fault associated lithospheric deformation (e.g. Biryol et al., 2010; Faccenna et al., 2014). However, a two-layer anisotropy inversion reveals that the lithospheric fast axis is fault-parallel in a > 80 km belt around the western part of fault, indicating a relatively wide shear zone (Merry et al., 2021).

Global observations suggest that shear zones can be detected by *XKS* shear wave splitting with widths ranging from $<$ 40 km to $\sim$200 km. And given that faults with a length of $\sim$100 km (Gao et al., 2019) can still display shear zones with a width of over 20 km, it is likely that shearing beneath the brittle portion of fault zones is commonly distributed over tens to hundreds of kilometers.

In many cases, plate motion, asthenospheric deformation, and fossil lithospheric deformation may also be aligned with the fault strike (e.g. Y. Li et al., 2011; Schulte-Pelkum et al., 2021), making the interpretation of splitting results nonunique. Processes causing splitting may be differentiated via further analysis of layered anisotropy structure, integration of other types of observations, and focusing particularly on parts of the fault that are oblique to the plate motion.

Many published individual event measurements appear to have back-azimuths close to the measured fast axis (Barak & Klemperer, 2016; Jiang et al., 2018; Gao et al., 2019; Merry et al., 2021). Extra caution should be taken in this case since the edge effects can produce erroneous measurements that should not be interpreted, as discussed in Section 4.2. These erroneous signals may also suggest the potential advantage to study the anisotropy structure using some types of waveform inversion to have a more complete consideration of different seismic wave behaviors (Ryberg et al., 2005), instead of relying on the less stable splitting measurements.

5 Conclusions

We analyzed synthetic shear wave splitting measurements for different fault zone (shear zone) settings for teleseismic core shear waves. Our analysis shows that shear zones wider than the Fresnel zone of about 80 km can be confidently identified, and splitting measurements made at their center likely reflect the true anisotropy structure of the lithospheric shear zone. Narrower width or more complex shear zones are more difficult to constrain. Detectability increases with the contrast in fast axis orientations between side

blocks and the shear zone, but individual measurements from different back-azimuths can still be unstable ~ 40 km around the shear zone core

Near the edge of the shear zone and regardless of its width, back-azimuth dependent erroneous measurements with large delay times and apparent fast axis orientations close to the back-azimuth appear due to the combined effect of anisotropy and scattering. Such erroneous measurements would be less prominent when the transition between the shear zone and the side block is spread out over a longer distance, again controlled by the length scale set by the Fresnel zone.

Our findings substantiate the importance of a good azimuthal coverage of earthquakes and cautions against interpretation of individual event splitting results. We also tested how a range of other factors such as epicentral distance, crustal thickness, source-time function period, sediment layer, asthenospheric anisotropy, and station distribution also affect the detectability of the shear zone. Shear zones below 10 km depth have to be at least 60 km wide to be confidently detected.

Based on the insights from the synthetics, we can reinterpret published splitting results from global transform faults. Those show evidence of distributed shear zones that are over 20 km wide, even when the fault itself is only 100 km long. This suggests that even confined crustal faults may be associated with shear deformation at large depths, and relative motion between tectonic blocks is likely not localized at the base of the lithosphere. Given that teleseismic shear wave splitting lacks depth sensitivity, joint analysis of receiver function and surface wave based anisotropy inversions should prove fruitful for further analysis of deformation in shear zones and the evolution of fault systems.

Open Research Section

Synthetic seismograms analyzed in this study are generated by RegHyM (Monteiller et al., 2021), a variant version of SPECFEM3D Cartesian (Komatitsch & Tromp, 2002). All information required for the simulation are provided in Model Setup and Methods sections. Wavefield simulation, model generation, and splitting measurement codes used in this study are available at Hua et al. (2025).

Acknowledgments

We thank S. Chevrot for discussions about wavefield simulations, G. Rümpker for comments on a previous version of this manuscript, and C.-C. Lee and M. Wiederspahn at UT for preliminary work and software support, respectively. We thank the editor D. Schmitt, the associate editor A.-A. Gabriel, and two anonymous reviewers for their constructive comments, which have improved this paper. J. Hua and T. W. Becker were partially supported by National Science Foundation awards EAR-1925939, 1927216, and 2045292.

References

Allison, K. L., & Dunham, E. M. (2021). Influence of shear heating and thermomechanical coupling on earthquake sequences and the brittle-ductile transition. *J. Geophys. Res.: Sol. Earth*, *126*(e2020JB021394).

Ando, M., Ishikawa, Y., & Yamasaki, F. (1983). Shear-wave polarization anisotropy in the mantle beneath Honshu, Japan. *J. Geophys. Res.: Sol. Earth*, *88*, 5850–5864.

Barak, S., & Klemperer, S. L. (2016). Rapid variation in upper-mantle rheology across the San Andreas fault system and Salton Trough, southernmost California, USA. *Geology*, *44*, 575–578.

Becker, T. W., Lebedev, S., & Long, M. D. (2012). On the relationship between az-

imuthal anisotropy from shear wave splitting and surface wave tomography. *J. Geophys. Res.: Sol. Earth*, *117*(B01306). (Original and updated splitting data base at `http://www-udc.ig.utexas.edu/external/becker/sksdata.html`) doi: 10.1029/2011JB008705

Behn, M. D., Lin, J., & Zuber, M. T. (2002). Evidence for weak oceanic transform faults. *Geophys. Res. Lett.*, *29*(24). doi: 10.1029/2002GL015612

Biryol, C. B., Zandt, G., Beck, S. L., Ozacar, A. A., Adiyaman, H. E., & Gans, C. R. (2010). Shear wave splitting along a nascent plate boundary: the North Anatolian Fault Zone. *Geophys. J. Int.*, *181*, 1201–1213.

Bolton, A. R., Schutt, D. L., Aster, R. C., Audet, P., Schaeffer, A. J., Estève, C., ... Cubley, J. F. (2022). Evidence for asthenospheric flow rotation in northwest Canada: insights from shear wave splitting. *Geophysical Journal International*, *228*(3), 1780–1792.

Bonnin, M., Tommasi, A., Hassani, R., Chevrot, S., Wookey, J., & Barruol, G. (2012). Numerical modelling of the upper-mantle anisotropy beneath a migrating strike-slip plate boundary: the San Andreas Fault system. *Geophys. J. Int.*, *191*, 436–458.

Browaeys, J., & Chevrot, S. (2004). Decomposition of the elastic tensor and geophysical applications. *Geophys. J. Int.*, *159*, 667–678.

Chevrot, S. (2000). Multichannel analysis of shear wave splitting. *J. Geophys. Res.: Sol. Earth*, *105*, 21579–21590.

Chevrot, S., Favier, N., & Komatitsch, D. (2004). Shear wave splitting in three-dimensional anisotropic media. *Geophys. J. Int.*, *159*, 711-720.

Chevrot, S., & van der Hilst, R. D. (2003). On the effects of a dipping axis of symmetry on shear wave splitting measurements. *Geophys. J. Int.*, *152*, 497–505.

Cocco, M., Aretusini, S., Cornelio, C., Nielsen, S. B., Spagnuolo, E., Tinti, E., & Di Toro, G. (2023). Fracture energy and breakdown work during earthquakes. *Ann. Rev. Earth Planet. Sci.*, *51*, 217–252.

Faccenna, C., Becker, T. W., Auer, L., Billi, A., Boschi, L., Brun, J.-P., ... Serpelloni, E. (2014). Mantle dynamics in the Mediterranean. *Rev. Geophys.*, *52*, 283–332.

Ford, H. A., Fischer, K. M., & Lekić, V. (2014). Localized shear in the deep lithosphere beneath the San Andreas fault system. *Geology*, *42*, 295–298.

Frederiksen, A., & Bostock, M. (2000). Modelling teleseismic waves in dipping anisotropic structures. *Geophys. J. Int.*, *141*, 401–412.

Fukao, Y. (1984). Evidence from core-reflected shear waves for anisotropy in the Earth's mantle. *Nature*, *371*, 149–151.

Gao, Y., Chen, L., Wang, X., & Ai, Y. (2019). Complex lithospheric deformation in eastern and northeastern Tibet from shear wave splitting observations and its geodynamic implications. *J. Geophys. Res.: Sol. Earth*, *124*, 10331–10346.

Hartog, R., & Schwartz, S. Y. (2001). Depth-dependent mantle anisotropy below the San Andreas fault system: Apparent splitting parameters and waveforms. *J. Geophys. Res.: Sol. Earth*, *106*, 4155–4168.

Hua, J., Fischer, K. M., & Savage, M. K. (2018). The lithosphere–asthenosphere boundary beneath the South Island of New Zealand. *Earth Planet. Sci. Lett.*, *484*, 92–102.

Hua, J., Schulte-Pelkum, V., Becker, T., He, B., & Zhu, H. (2025, June). *3d (x)ks shear wave splitting modeling near fault zones [software].* Zenodo. Retrieved from `https://doi.org/10.5281/zenodo.15710096` doi: 10.5281/zenodo.15710096

Jiang, C., Schmandt, B., & Clayton, R. W. (2018). An anisotropic contrast in the lithosphere across the central San Andreas fault. *Geophys. Res. Lett.*, *45*, 3967–3975.

Karalliyadda, S., Savage, M., Sheehan, A., Collins, J., Zietlow, D., & Shelley, A. (2015). S-wave splitting in the offshore South Island, New Zealand: Insights

into plate-boundary deformation. *Geochem., Geophys., Geosys.*, *16*, 2829–2847.

Kaviani, A., Rümpker, G., Weber, M., & Asch, G. (2011). Short-scale variations of shear-wave splitting across the Dead Sea basin: Evidence for the effects of sedimentary fill. *Geophys. Res. Lett.*, *38*(4). doi: 10.1029/2010GL046464

Kennett, B., & Engdahl, E. (1991). Traveltimes for global earthquake location and phase identification. *Geophys. J. Int.*, *105*, 429–465.

Komatitsch, D., & Tromp, J. (2002). Spectral-element simulations of global seismic wave propagation—II. Three-dimensional models, oceans, rotation and self-gravitation. *Geophys. J. Int.*, *150*, 303–318.

Levin, V., Okaya, D., & Park, J. (2007). Cause and effect: Shear wave birefringence in wedge-shaped anisotropic regions. *Geophys. J. Int.*, *168*, 275–286.

Li, Y., Wu, Q., Zhang, F., Feng, Q., & Zhang, R. (2011). Seismic anisotropy of the Northeastern Tibetan Plateau from shear wave splitting analysis. *Earth Planet. Sci. Lett.*, *304*, 147–157.

Li, Y.-G., & Leary, P. (1990). Fault zone trapped seismic waves. *Bull. Seismol. Soc. Am.*, *80*, 1245–1271.

Little, T. A., Savage, M. K., & Tikoff, B. (2002). Relationship between crustal finite strain and seismic anisotropy in the mantle, Pacific-Australia plate boundary zone, South Island, New Zealand. *Geophys. J. Int.*, *151*, 106–116.

Long, M. D., & Becker, T. W. (2010). Mantle dynamics and seismic anisotropy. *Earth Planet. Sci. Lett.*, *297*, 341-354.

Long, M. D., de Hoop, M. V., & van der Hilst, R. D. (2008). Wave equation shear wave splitting tomography. *Geophys. J. Int.*, *172*, 311–330.

Long, M. D., & Silver, P. G. (2009). Shear wave splitting and mantle anisotropy: Measurements, interpretations, and new directions. *Surv. Geophys.*, *30*, 407–461.

Mark, H. F. (2024). Refining the extent and depth of the shear zone surrounding the alpine fault using receiver function harmonics. *Geophysical Research Letters*, *51*(23), e2024GL112092.

Martelat, J.-E., Schulmann, K., Lardeaux, J.-M., Nicollet, C., & Cardon, H. (1999). Granulite microfabrics and deformation mechanisms in southern Madagascar. *Journal of Structural Geology*, *21*(6), 671–687.

Merry, T. A., Bastow, I. D., Kounoudis, R., Ogden, C. S., Bell, R. E., & Jones, L. (2021). The influence of the North Anatolian Fault and a fragmenting slab architecture on upper mantle seismic anisotropy in the eastern Mediterranean. *Geochem., Geophys., Geosys.*, *22*, e2021GC009896.

Montagner, J.-P., & Anderson, D. L. (1989). Petrological constraints on seismic anisotropy. *Phys. Earth Planet. Inter.*, *54*, 82–105.

Montagner, J.-P., Griot-Pommera, D.-A., & Lavé, J. (2000). How to relate body wave and surface wave anisotropy? *J. Geophys. Res.: Sol. Earth*, *105*, 19015–19027.

Monteiller, V., Beller, S., Plazolles, B., & Chevrot, S. (2021). On the validity of the planar wave approximation to compute synthetic seismograms of teleseismic body waves in a 3-D regional model. *Geophys. J. Int.*, *224*, 2060–2076.

Monteiller, V., & Chevrot, S. (2010). How to make robust splitting measurements for single-station analysis and three-dimensional imaging of seismic anisotropy. *Geophys. J. Int.*, *182*, 311–328.

Monteiller, V., & Chevrot, S. (2011). High-resolution imaging of the deep anisotropic structure of the San Andreas Fault system beneath southern California. *Geophys. J. Int.*, *182*, 418–446.

Norris, R. J., & Toy, V. G. (2014). Continental transforms: A view from the Alpine Fault. *J. Struct. Geol.*, *64*, 3–31.

Reiss, M. C., & Rümpker, G. (2017). SplitRacer: MATLAB Code and GUI for Semiautomated Analysis and Interpretation of Teleseismic Shear-Wave Split-

ting. *Seis. Res. Lett.*, *88*, 392–409.

Reiss, M. C., Rümpker, G., Tilmann, F., Yuan, X., Giese, J., & J., R. E. (2016). Seismic anisotropy of the lithosphere and asthenosphere beneath southern Madagascar from teleseismic shear wave splitting analysis and waveform modeling. *J. Geophys. Res.: Sol. Earth*, *121*, 6627–6643. doi: 10.1002/2016JB013020

Rümpker, G., Kaviani, A., Link, F., Reiss, M. C., & Komeazi, A. (2023). Testing observables for teleseismic shear-wave splitting inversions: ambiguities of intensities, parameters, and waveforms. *Annals Geophys.*, *66*, SE206–SE206.

Rümpker, G., & Ryberg, T. (2000). New "Fresnel-zone" estimates for shear-wave splitting observations from finite-difference modeling. *Geophys. Res. Lett.*, *27*, 2005–2008.

Rümpker, G., Ryberg, T., Bock, G., & Desert Seismology Group. (2003). Boundary-layer mantle flow under the Dead Sea transform fault inferred from seismic anisotropy. *Nature*, *425*, 497–501.

Rümpker, G., & Silver, P. G. (1998). Apparent shear-wave splitting parameters in the presence of vertically varying anisotropy. *Geophys. J. Int.*, *135*, 790–800.

Ryberg, T., Rümpker, G., Haberland, C., Stromeyer, D., & Weber, M. (2005). Simultaneous inversion of shear wave splitting observations from seismic arrays. *J. Geophys. Res.: Sol. Earth*, *110*(B03301). doi: 10.1029/2004JB003303

Savage, M. K. (1998). Lower crustal anisotropy or dipping boundaries? Effects on receiver functions and a case study in New Zealand. *J. Geophys. Res.: Sol. Earth*, *103*, 15069–15087.

Savage, M. K., Fischer, K. M., & Hall, C. E. (2004). Strain modelling, seismic anisotropy and coupling at strike-slip boundaries: Applications in New Zealand and the San Andreas fault. In J. Grocott, B. Tikoff, K. J. W. McCaffrey, & G. Taylor (Eds.), *Vertical coupling and decoupling in the lithosphere* (Vol. 227, pp. 9–40). London: Geological Society of London.

Schulte-Pelkum, V., Becker, T. W., Behr, W. M., & Miller, M. S. (2021). Tectonic inheritance during plate boundary evolution in southern California constrained from seismic anisotropy. *Geochem., Geophys., Geosys.*, *22*, e2021GC010099. doi: 10.1029/2021GC010099

Sibson, R. H. (1983). Continental fault structure and the shallow earthquake source. *J. Geol. Soc.*, *140*, 741–767.

Šíleny, J., & Plomerová, J. (1996). Inversion of shear-wave splitting parameters to retrieve three-dimensional orientation of anisotropy in continental lithosphere. *Phys. Earth Planet. Inter.*, *95*, 277–292.

Silver, P. G. (1996). Seismic anisotropy beneath the continents: Probing the depths of geology. *Ann. Rev. Earth Planet. Sci.*, *24*, 385–432.

Silver, P. G., & Chan. (1991). Shear wave splitting and subcontinental mantle deformation. *J. Geophys. Res.: Sol. Earth*, *96*, 16429–16454.

Silver, P. G., & Savage, M. K. (1994). The interpretation of shear wave splitting parameters in the presence of two anisotropic layers. *Geophys. J. Int.*, *119*, 949–963.

Tong, P., Komatitsch, D., Tseng, T.-L., Hung, S.-H., Chen, C.-W., Basini, P., & Liu, Q. (2014). A 3-d spectral-element and frequency-wave number hybrid method for high-resolution seismic array imaging. *Geophys. Res. Lett.*, *41*, 7025–7034.

Vauchez, A., Tommasi, A., & Mainprice, D. (2012). Faults (shear zones) in the Earth's mantle. *Tectonophys.*, *558*, 1–27.

Vinnik, L., Kosarev, G. L., & Makeyeva, L. I. (1984). Anisotropy of the lithosphere from the observations of SKS and $SKKS$ phases. *Proc. Acad. Sci. USSR*, *278*, 1335–1339.

Yang, H., Zhu, L., & Cochran, E. S. (2011). Seismic structures of the Calico fault zone inferred from local earthquake travel time modelling. *Geophys. J. Int.*, *186*, 760–770.

Zietlow, D. W., Sheehan, A. F., Molnar, P. H., Savage, M. K., Hirth, G., Collins, J. A., & Hager, B. H. (2014). Upper mantle seismic anisotropy at a strike-slip boundary: South Island, New Zealand. *J. Geophys. Res.: Sol. Earth*, *119*, 1020–1040.

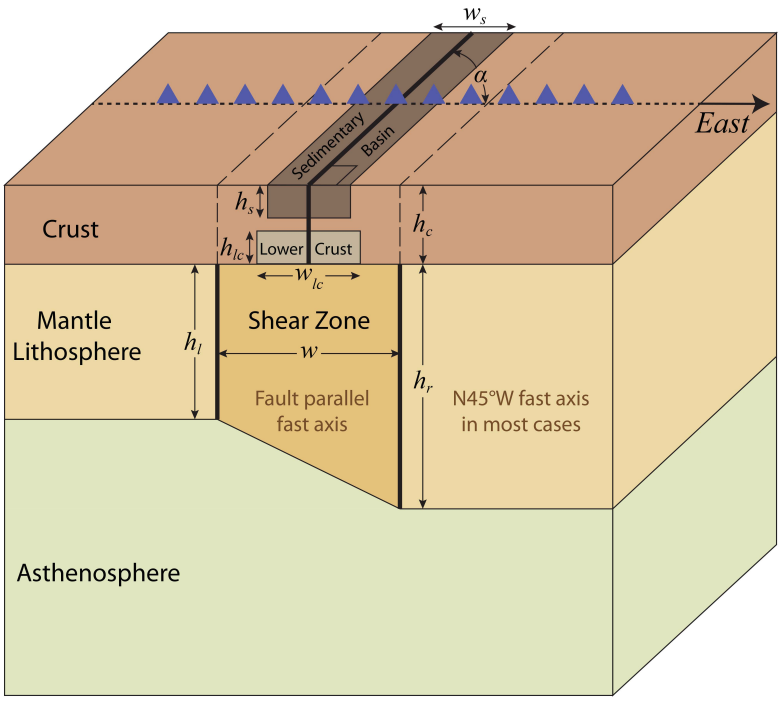

Figure 1. Schematic of the model setup. The model contains three layers, an isotropic crust, an isotropic/anisotropic mantle lithosphere, and an isotropic/anisotropic asthenosphere. The fault is assumed to have infinitely small width in the crust, while in the mantle lithosphere, an anisotropic shear zone is centered beneath the fault with a finite width. The linear surface seismic array (blue triangles) is always aligned in the East-West orientation, and the fault is mostly North-South oriented except for one case. In two cases, a sedimentary basin or an anisotropic lower crustal shear zone were added. Model-related parameters are labeled.

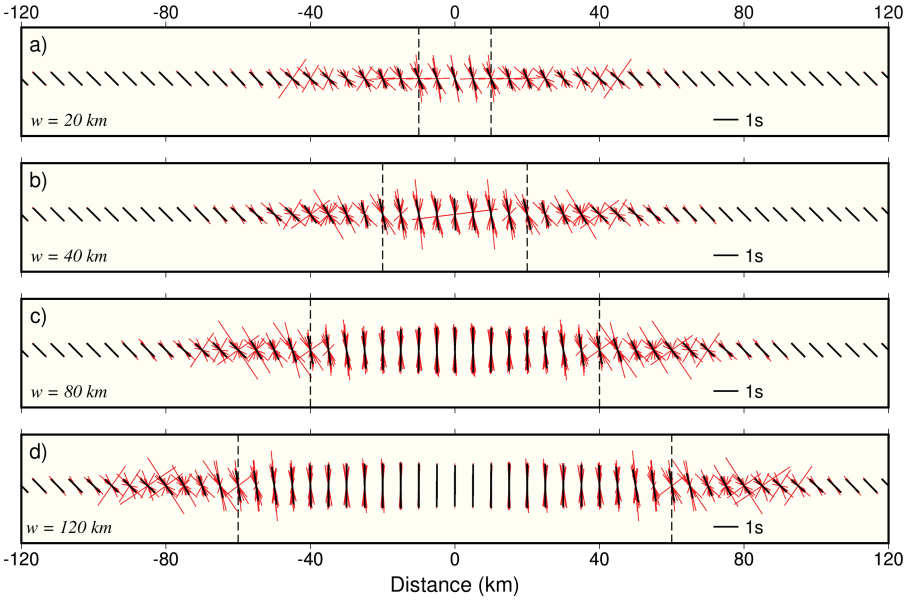

Figure 2. Splitting measurements for shear zones with different widths. In these cases, the isotropic crust is 35 km thick, and $h_l = h_r = 65$ km. The asthenosphere is isotropic. The anisotropic shear zone has the fast axis pointing to the north, and side blocks have fast axes pointing to N45°W; x-axes show distance along the linear array. (a)-(d) are for shear zones with widths of 20, 40, 80, and 120 km, and edges of the shear zone are marked by black dashed lines. Splitting measurements are shown every 5 km. While red bars show individual measurements for different back-azimuths, the black bar shows the median measurement from different back-azimuths when the number of useful measurements is larger than five. Bars are aligned with the fast axis orientation and scaled by the delay time (1 s delay time labeled).

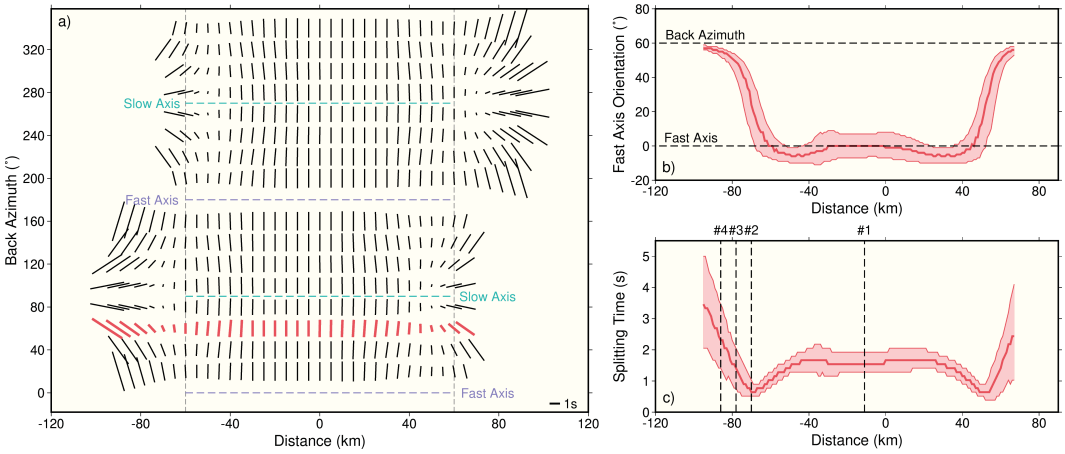

Figure 3. Erroneous splitting measurements around the edge of the shear zone. (a) Splitting measurements for a case where only the 120 km wide shear zone is anisotropic. The setup is identical to the case of Figure 2d besides the side blocks are isotropic. Bars show splitting measurements at different locations (x-axis) and from incoming waves with different back-azimuths (y-axis). Edges of the shear zone are marked by black dashed lines, and fast and slow axes orientations of the media are marked by blue and green dashed lines. Measurements are made every 5 km and 20°, and an absence of the bar represents null measurement. (b) Measured fast axis orientation variation with distance for the back-azimuth of 60° (red line, also marked in red in a). The red shade shows the 95% confidence level of the measurement. The actual fast-axis orientation of the shear zone and the back-azimuth direction are shown by black dashed lines. (c) Similar to (b) but showing the measured delay time variation. Locations of four reference points in Figure 4 are marked by black dashed lines.

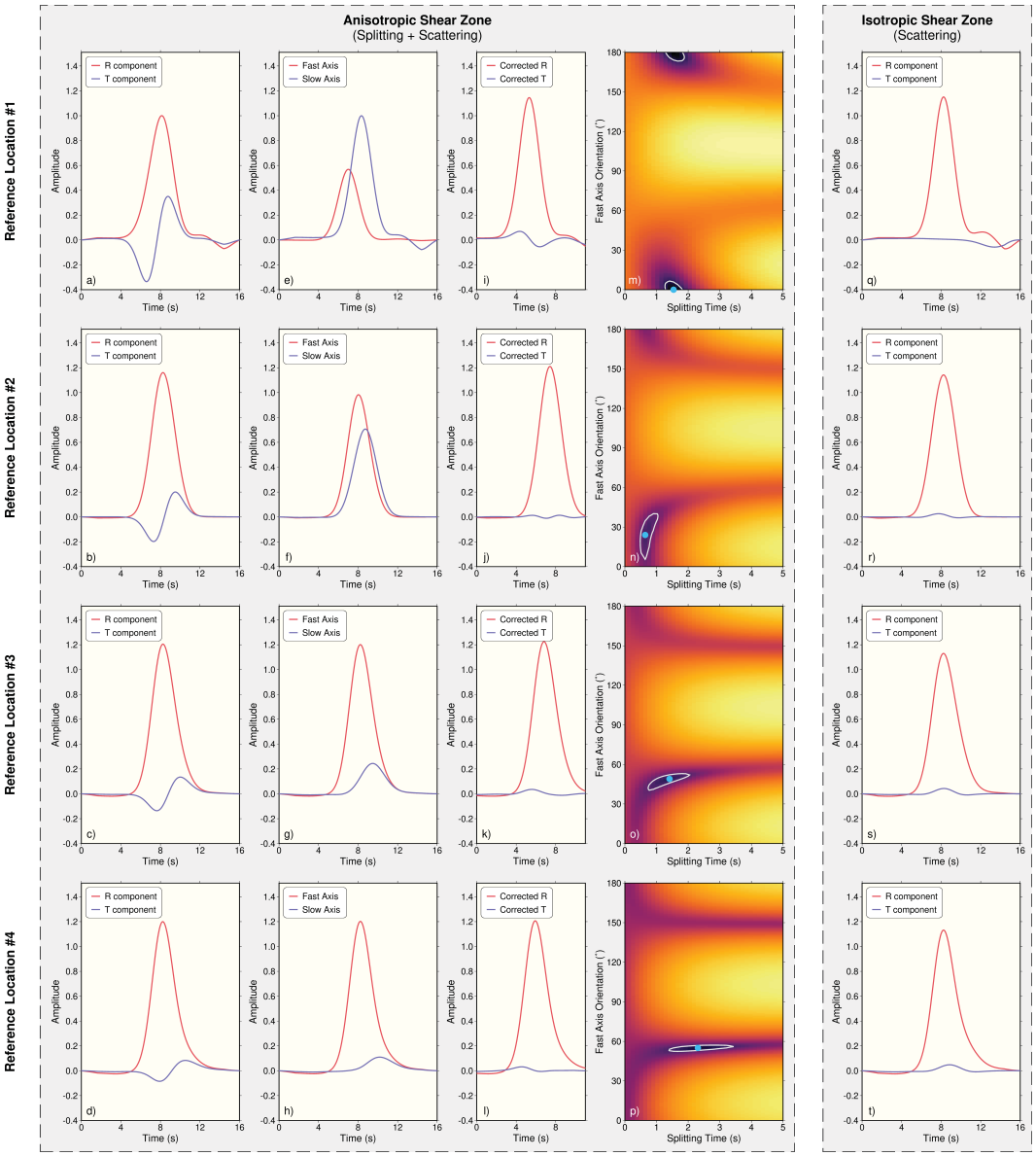

Figure 4. The influence of shear zone anisotropy and scattering on erroneous measurements. The four rows from top to bottom are for locations close to the center of the shear zone (#1 at −11 km in Figure 3c), and near the edge of the shear zone where misleading measurements occur (#2/#3/#4 at −70/−78/−86 km in Figure 3c). While left four columns are based on the same structure as the case in Figure 3, the fifth column corresponds to a case where the shear zone is modified to be isotropic, and its V_S is equal to V_S along the slow axis for the shear zone in Figure 3. The first and fifth columns show observed radial (R) and transverse (T) components of the incoming wave. The second column shows seismograms along fast and slow axes according to the splitting measurement. The third column shows the corrected R and T components before splitting based on the measurement. The fourth column shows T component energies (log-scale) before splitting assuming different delay times and fast axis orientations, and the optimal result (cyan dot) is picked at where the energy is minimized (darkest color). 95% confidence level is shown by the white line.

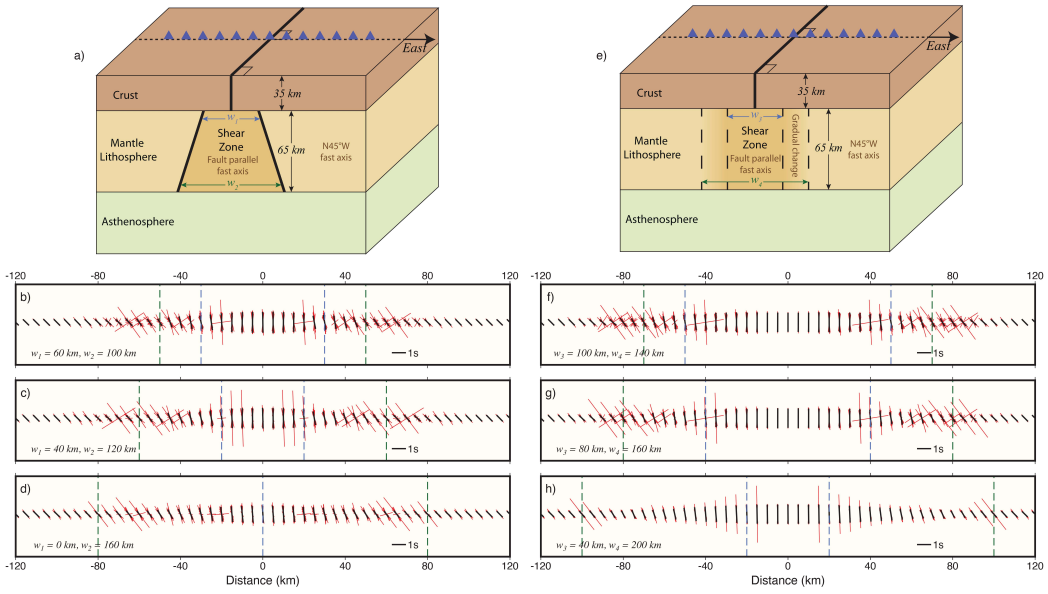

Figure 5. The influence of the shear zone - background lithosphere transition. The left column is for cases with dipping shear zone edges, and the right column is for cases with a gradual transition between the shear zone and the side block. The model setups for the cases are shown by schematics in the top row with related parameters labeled, and shear zones are symmetric with respect to the fault plane. (b)-(d) are comparable to Figure 2c, but for the setup in (a), with w_1 set to 60, 40 and 0 km, and w_2 set to 100, 120 and 160 km. (f)-(h) are comparable to Figure 2d, but for the setup in (e), with w_1 set to 100, 80 and 40 km, and w_2 set to 140, 160 and 200 km.

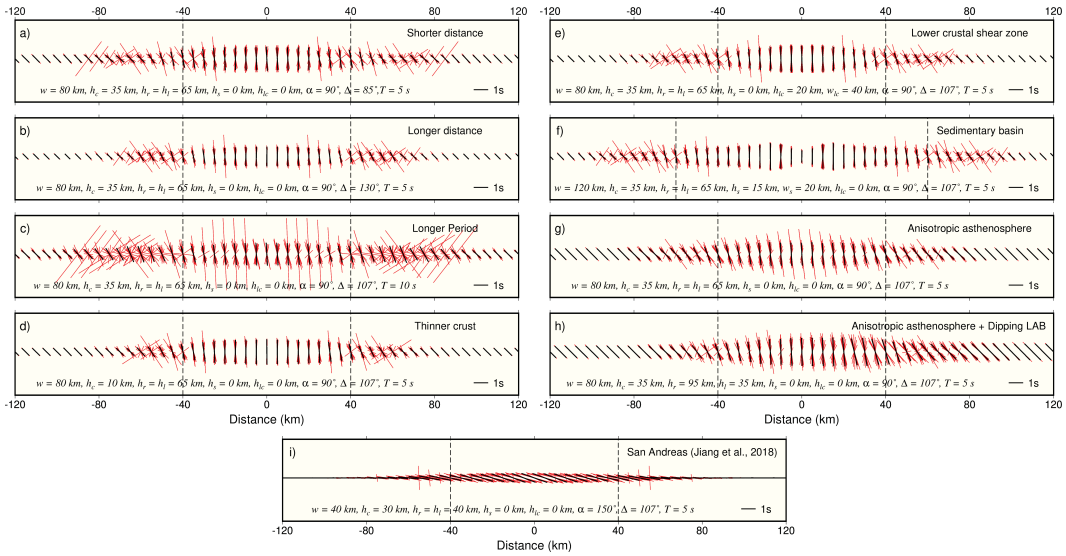

Figure 6. Influence of incoming waveform features on splitting measurements. The panels are similar to those derived from the reference model (Figure 2c), but for different model parameters, as labeled. (a) and (b) show results for epicentral distances (Δ) of 85° and 130°. (c) and (d) use a source wavelet with a longer period and thin the crust compared to the reference. (e) adds a lower crustal shear zone. (f) is similar to the case in Figure 2d, but adds a sedimentary basin (Figure 1) around the fault. (g) is based on the reference of Figure 2c, with an anisotropic asthenosphere included. (h) is based on (g), but the LAB is dipping beneath the shear zone. (i) is the only case where the fast axes azimuth α is not 90° (cf. Figure 1), and is designed to mimic the setup near the San Andreas Fault based on Jiang et al. (2018).

Figure 1.

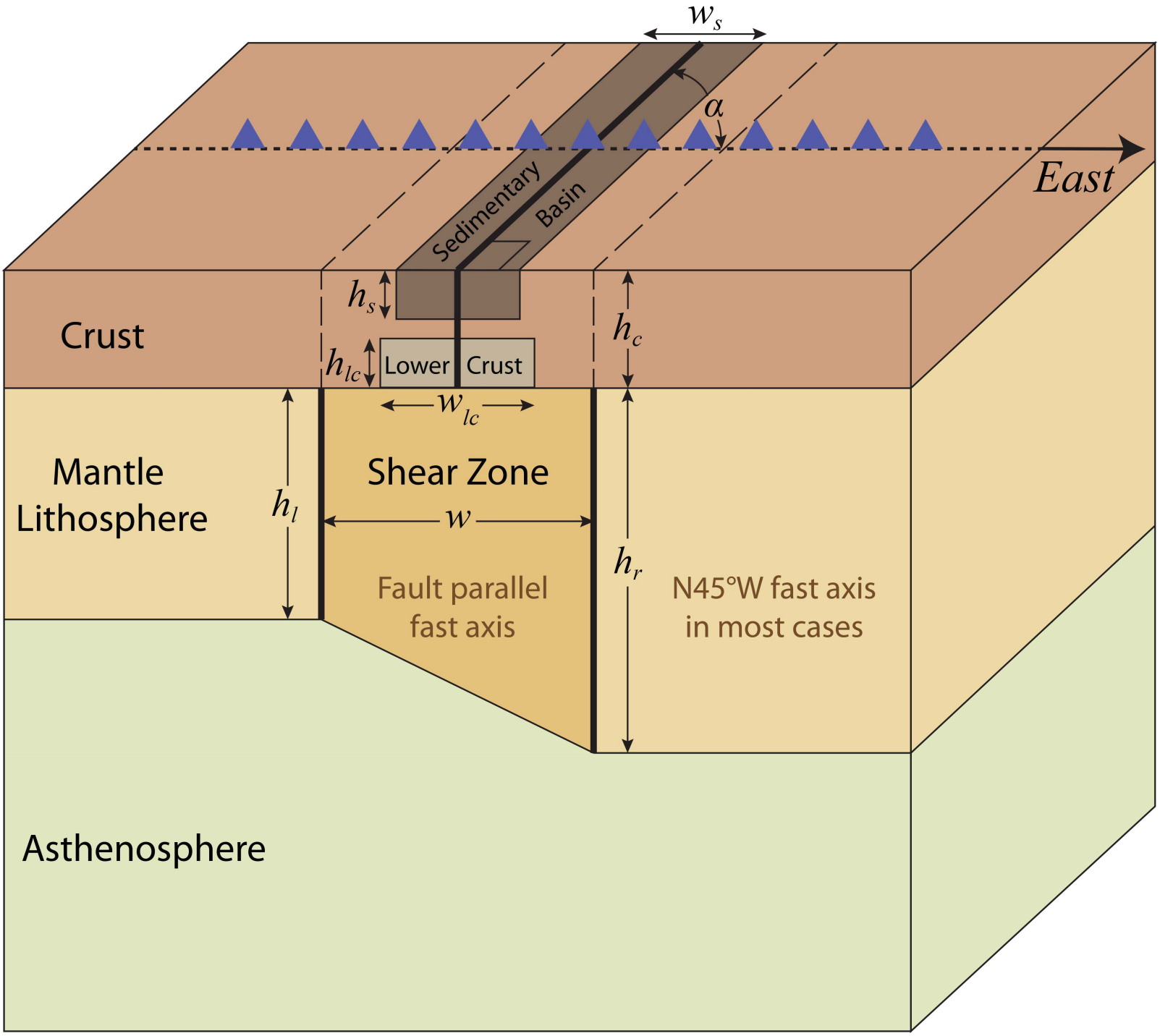

In press at JGR-SE, August 2025.

Figure 2.

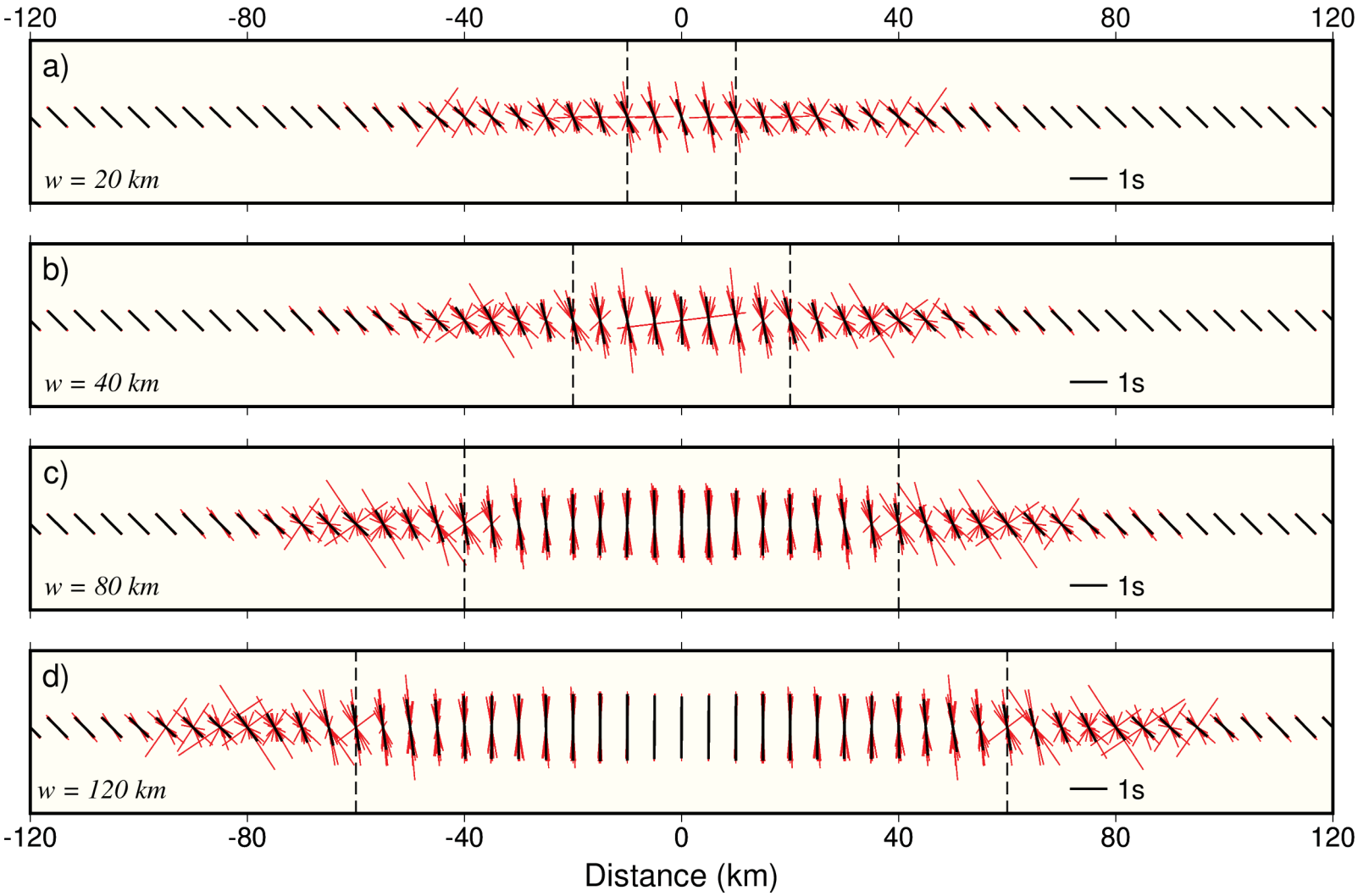

In press at JGR-SE, August 2025.

Figure 3.

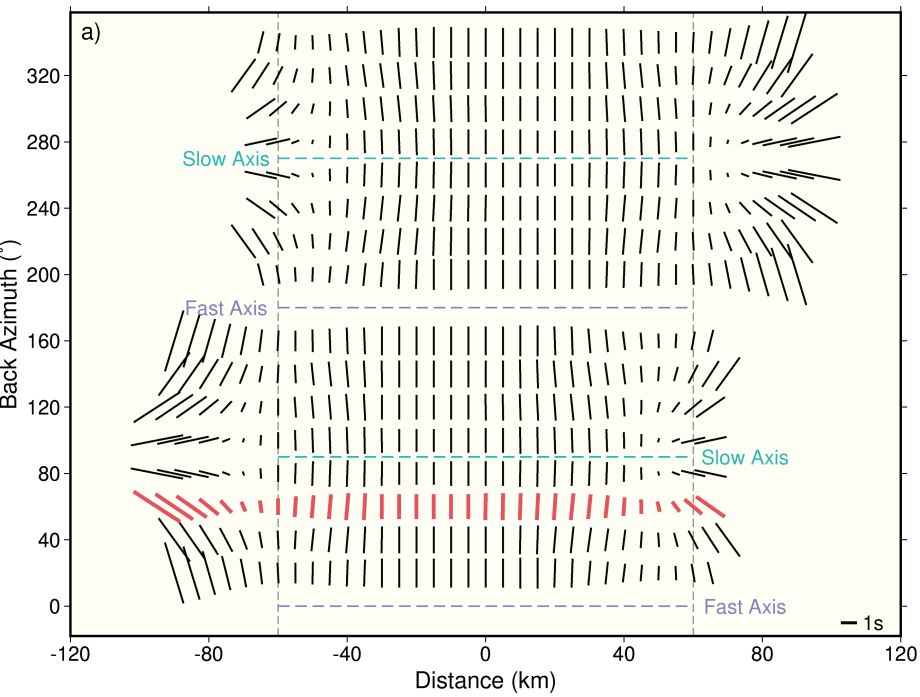
a)
Slow Axis
Fast Axis
Slow Axis
Fast Axis
1s
Back Azimuth (°)
Distance (km)

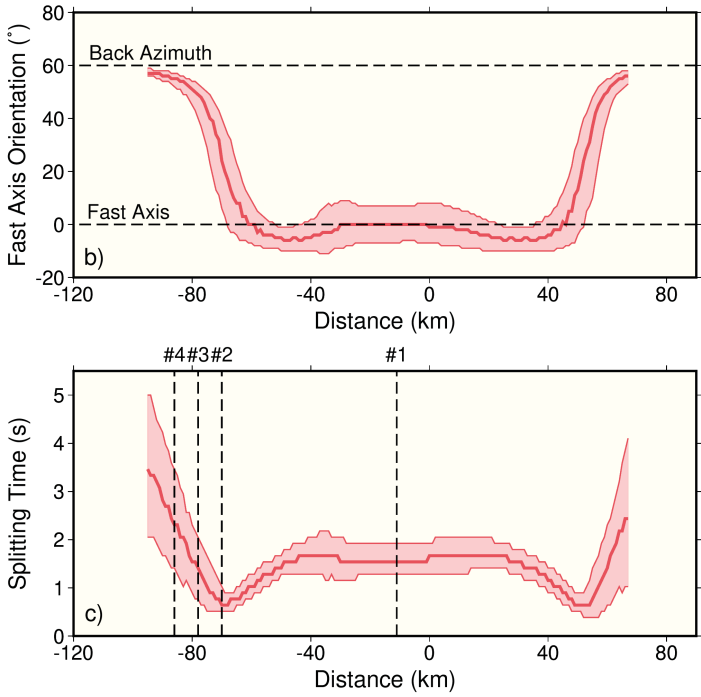
Back Azimuth
Fast Axis
b)
Fast Axis Orientation (°)
Distance (km)
#4#3#2
#1
c)
Splitting Time (s)
Distance (km)

Figure 4.

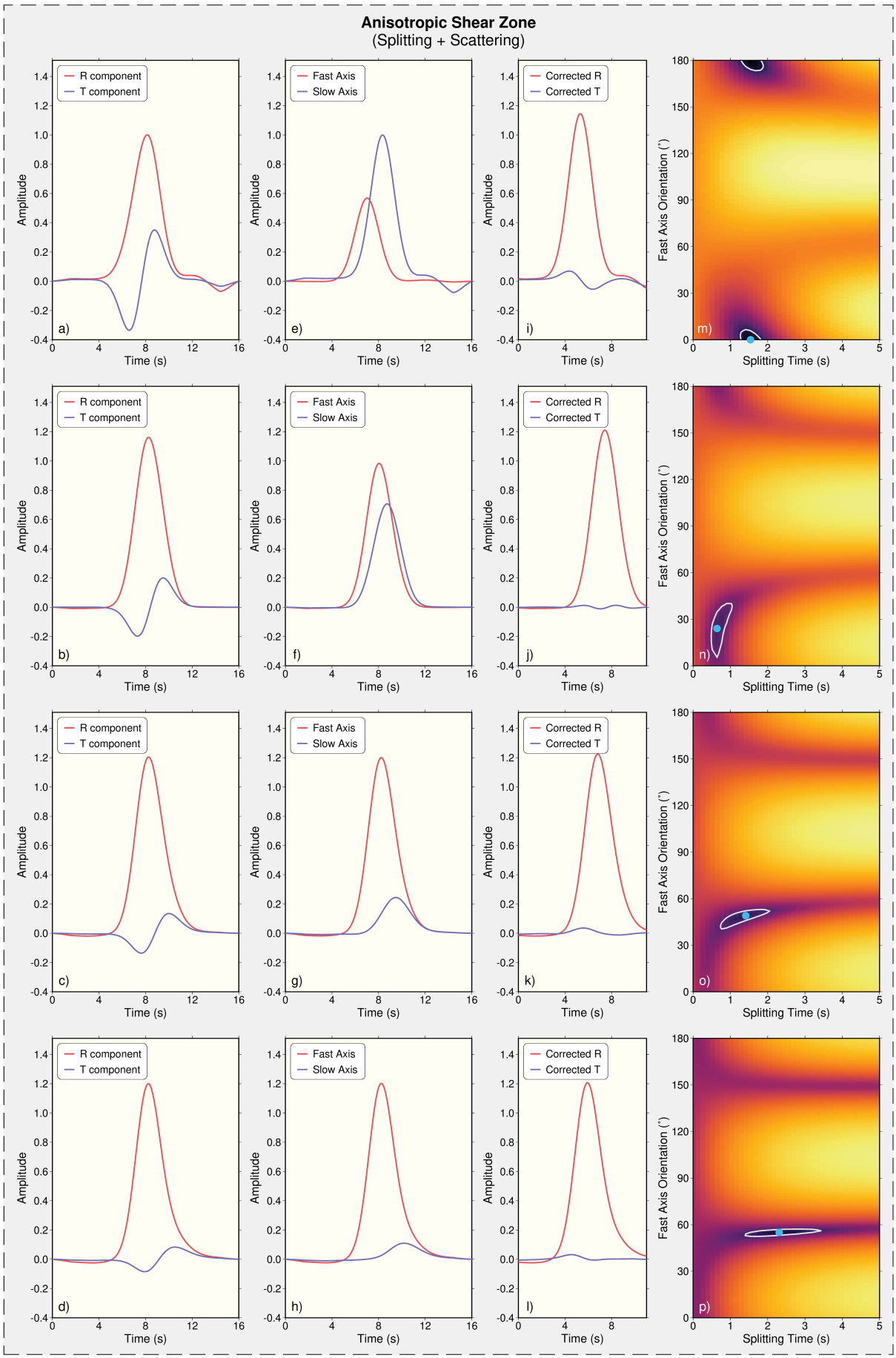

In press at JGR-SE, August 2025.

Figure 5.

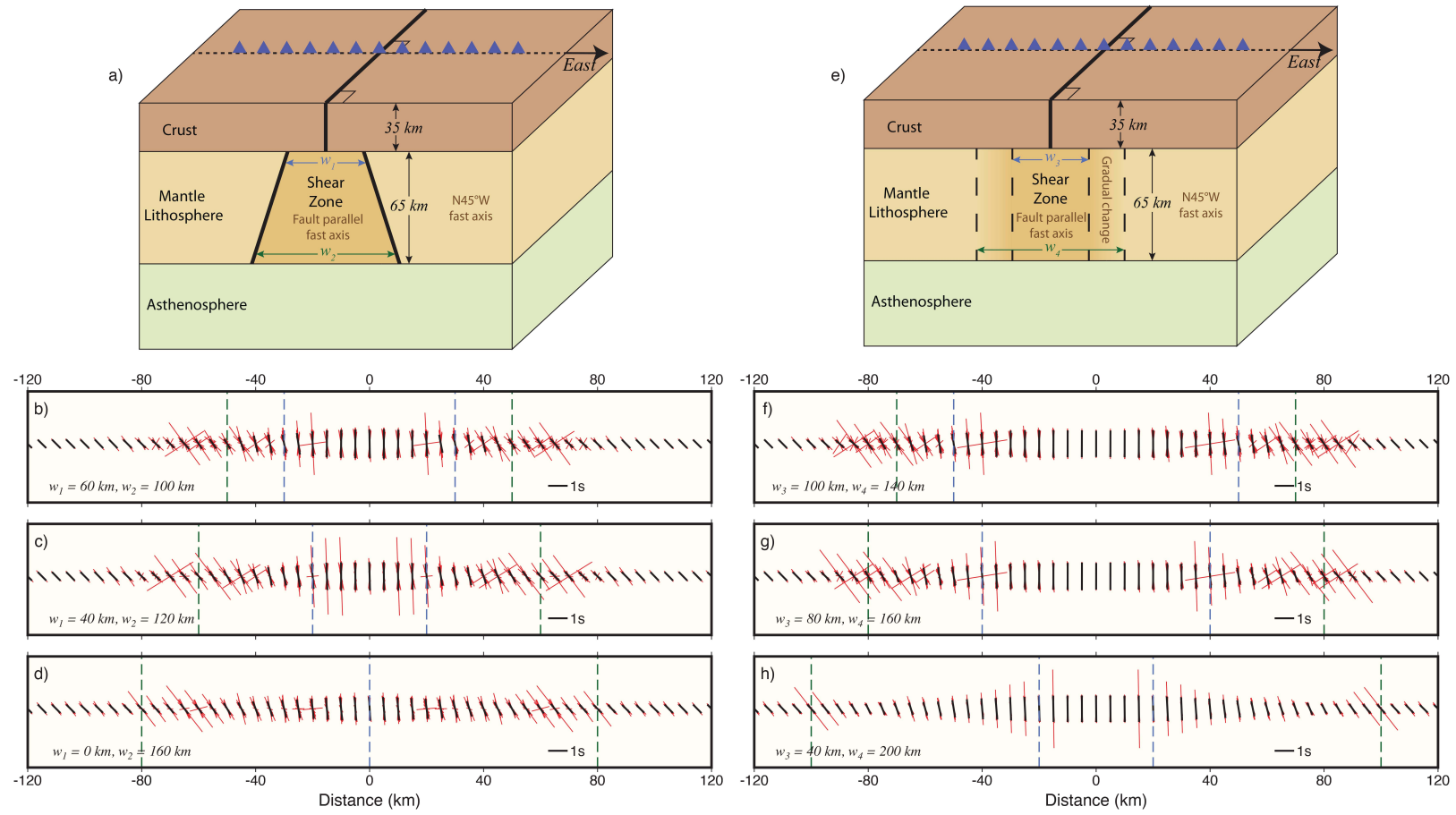
a)
East
Crust
35 km
Mantle
Lithosphere
Shear
Zone
Fault parallel
fast axis
65 km
N45°W
fast axis
Asthenosphere
e)
East
Crust
35 km
Mantle
Lithosphere
Shear
Zone
Fault parallel
fast axis
Gradual change
65 km
N45°W
fast axis
Asthenosphere
b)
w1 = 60 km, w2 = 100 km
1s
c)
w1 = 40 km, w2 = 120 km
1s
d)
w1 = 0 km, w2 = 160 km
1s
f)
w3 = 100 km, w4 = 140 km
1s
g)
w3 = 80 km, w4 = 160 km
1s
h)
w3 = 40 km, w4 = 200 km
1s
-120
-80
-40
0
40
80
120
Distance (km)

Figure 6.

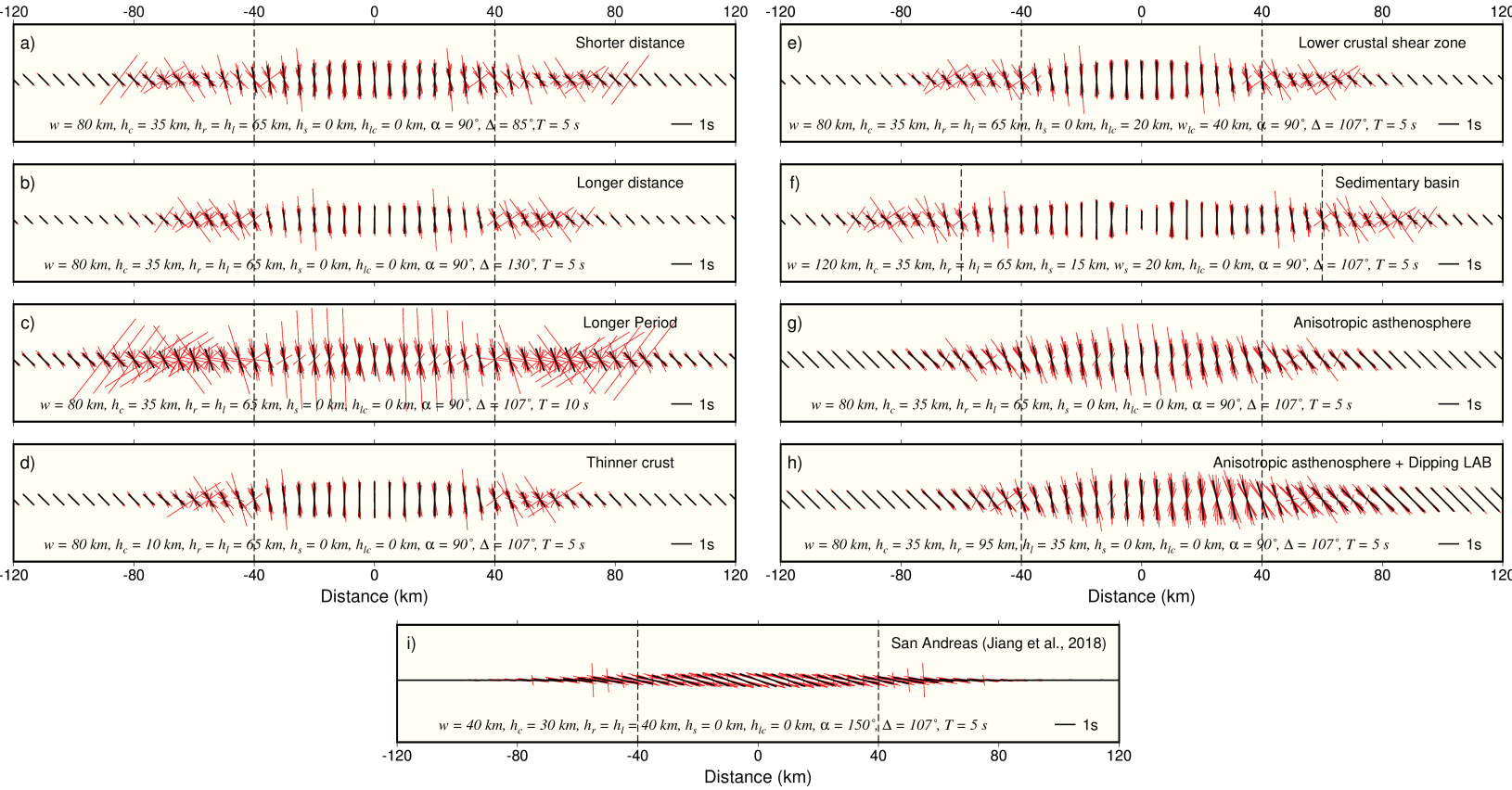
a)
Shorter distance
w = 80 km, h_c = 35 km, h_r = h_l = 65 km, h_s = 0 km, h_lc = 0 km, α = 90°, Δ = 85°, T = 5 s
1s
b)
Longer distance
w = 80 km, h_c = 35 km, h_r = h_l = 65 km, h_s = 0 km, h_lc = 0 km, α = 90°, Δ = 130°, T = 5 s
1s
c)
Longer Period
w = 80 km, h_c = 35 km, h_r = h_l = 65 km, h_s = 0 km, h_lc = 0 km, α = 90°, Δ = 107°, T = 10 s
1s
d)
Thinner crust
w = 80 km, h_c = 10 km, h_r = h_l = 65 km, h_s = 0 km, h_lc = 0 km, α = 90°, Δ = 107°, T = 5 s
1s
-120 -80 -40 0 40 80 120
Distance (km)
e)
Lower crustal shear zone
w = 80 km, h_c = 35 km, h_r = h_l = 65 km, h_s = 0 km, h_lc = 20 km, w_lc = 40 km, α = 90°, Δ = 107°, T = 5 s
1s
f)
Sedimentary basin
w = 120 km, h_c = 35 km, h_r = h_l = 65 km, h_s = 15 km, w_s = 20 km, h_lc = 0 km, α = 90°, Δ = 107°, T = 5 s
1s
g)
Anisotropic asthenosphere
w = 80 km, h_c = 35 km, h_r = h_l = 65 km, h_s = 0 km, h_lc = 0 km, α = 90°, Δ = 107°, T = 5 s
1s
h)
Anisotropic asthenosphere + Dipping LAB
w = 80 km, h_c = 35 km, h_r = 95 km, h_l = 35 km, h_s = 0 km, h_lc = 0 km, α = 90°, Δ = 107°, T = 5 s
1s
-120 -80 -40 0 40 80 120
Distance (km)

i)
San Andreas (Jiang et al., 2018)
w = 40 km, h_c = 30 km, h_r = h_l = 40 km, h_s = 0 km, h_lc = 0 km, α = 150°, Δ = 107°, T = 5 s
1s
-120 -80 -40 0 40 80 120
Distance (km)